RESEARCH ARTICLE

Key Points:
- Birkeland currents from AMPERE mission are used to drive the TIE-GCM
- Ionospheric conductivities are made consistent with enhanced upward currents
- Agreement is found with existing conductance model and ground magnetic data

Correspondence to:
S. Marsal,
smarsal@obsebre.es

Conductivities consistent with Birkeland currents in the AMPERE-driven TIE-GCM

S. Marsal[1]

[1]Observatori de l'Ebre, (OE), CSIC – Universitat Ramon Llull, Roquetes, Spain

Abstract The Active Magnetosphere and Planetary Electrodynamics Response Experiment (AMPERE) satellite mission has offered for the first time global snapshots of the geomagnetic field-aligned currents with unprecedented space and time resolution, thus providing an opportunity to feed an acknowledged first-principles model of the Earth's upper atmosphere such as the National Center for Atmospheric Research Thermosphere-Ionosphere-Electrodynamics General Circulation Model (NCAR TIE-GCM). In the first step, Marsal et al. (2012) used AMPERE data in the current continuity equation between the magnetosphere and the ionosphere to drive the TIE-GCM electrodynamics. In the present work, ionospheric conductivities have been made consistent with enhanced upward field-aligned currents, which are assumed to correspond to electrons plunging as a result of downward acceleration by electric fields built up along the geomagnetic field lines. The resulting conductance distribution is reasonably commensurate with an independent model that has tried to quantify the ionizing effect of precipitating particles onto the auroral ionosphere. On the other hand, comparison of geomagnetic observatory data with the ground magnetic variations output by the model only shows a modest improvement with respect to our previous approach.

1. Introduction

Electron precipitation in the auroral oval has long been known to be a major source for the production of electrical conductivity in the high-latitude ionosphere. This component, on the other hand, is the main charge carrier of upward geomagnetic field-aligned (or Birkeland) currents flowing between the ionosphere and the magnetosphere, exceeding the ion contribution typically by an order of magnitude [*Cattell et al.*, 1979; *Korth et al.*, 2014]. Thus, it is logical to assume a close relation between ionospheric conductivity and upward Birkeland current density.

Auroral precipitation and emission is conventionally divided into its diffuse and discrete forms. The former is known to be mainly produced by plasma sheet electrons that have undergone magnetospheric convection and subsequent pitch angle diffusion into the loss cone by interaction with whistler mode waves [*Ni et al.*, 2011a, 2011b]; the visible results of diffuse precipitation are vaguely confined, structureless luminous features in the nighttime auroral zone. The discrete aurora, on the other hand, consists of spatially confined apparitions with a more recognizable shape, often showing up dynamic structures, especially during magnetically disturbed conditions such as substorms. Although proton aurorae can also be observed, discrete auroras are mainly produced by higher-energy electrons with observed mean energies typically in the range 2–20 keV [*Fridman and Lemaire*, 1980]. Such energies require additional acceleration processes of the plasma sheet particles, since the characteristic energy in this magnetospheric region barely surpasses a few keV. Acceleration is produced either by magnetic field-aligned (or parallel) electric fields [*Knight*, 1973; *Evans*, 1974] or by dispersive Alfvén waves [e.g., *Chaston et al.*, 2003] and may take place somewhere along the magnetic field line, i.e., between about 1 R_E (Earth radius) or so above the auroral ionosphere and 10 R_E (near the central plane of the magnetotail).

In the theoretical field, *Knight* [1973] deduced expressions for the upward Birkeland current as a function of the field-aligned potential drop between the ionosphere and the magnetosphere assuming thermal distributions at either ends; *Evans* [1974] developed a model of the precipitating electron flux in which a magnetic field-aligned potential difference accelerates electrons downward toward the ionosphere; and *Fridman and Lemaire* [1980] and *Janhunen and Olsson* [1998] obtained number and energy fluxes in terms of this potential drop.

In the observational field, electron precipitation has been characterized by different authors, using either particle detectors [e.g., *McDiarmid et al.*, 1975; *Wallis and Budzinski*, 1981; *Spiro et al.*, 1982; *Hardy et al.*, 1987;

Newell et al., 2009] or auroral imagery [e.g., *Germany et al.*, 1997; *Zhang and Paxton*, 2008]. *Wallis and Budzinski* [1981] and *Spiro et al.* [1982] have produced mean conductivity models as a function of an auroral activity index (*Kp* or *AE*) by inserting the resulting electron spectral distributions either into energy deposition codes [*Rees*, 1963] or into simple expressions derived from them [e.g., *Vickrey et al.*, 1981; *Robinson et al.*, 1987]. *Newell et al.* [2009] have quantified the contribution of the different types of aurora as a linear function of a solar wind parameter in each (magnetic) latitude - local time bin.

Coupling of Birkeland currents with ionospheric conductivity enhancements has been made by others. *Mishin et al.* [1986], for example, assume that the height-integrated conductivity (or simply conductance) is contributed, at a given local time and for a given level of auroral magnetic activity, by a linear relationship depending on the instantaneous distribution of upward field-aligned currents calculated from the equivalent current function, which in turn is deduced from ground magnetic data. *Blomberg and Marklund* [1988] have examined the effects on the high-latitude convection pattern of a coupling with the conductance that is essentially proportional to the upward current density and have found considerable modification in the rotation of the entire potential pattern due to this fact. *Marklund et al.* [1988] have used essentially the same relationship between conductances and field-aligned currents to obtain snapshots of the auroral electrodynamics on a global scale by the use of satellite data.

A continuation of the work of *Marsal et al.* [2012] is presented here. In that paper, Birkeland currents measured by the Active Magnetosphere and Planetary Electrodynamics Response Experiment (AMPERE) were used in the current continuity equation to drive the Thermosphere-Ionosphere-Electrodynamics General Circulation Model (TIE-GCM). Unlike the approach considered in that paper, where the electric conductivity of the auroral ionosphere was considered to vary according to a geomagnetic activity index, the aim of this work is to take full advantage of the information provided by the AMPERE data set by introducing an explicit feedback between the field-aligned currents and the conductivity. In particular, ionospheric conductivities have been made consistent with enhanced upward field-aligned current sectors corresponding to electrons precipitating as a result of downward acceleration by electric fields that are parallel to the ambient magnetic field. Based on the work of *Knight* [1973], expressions relating the upward current at the top of the ionosphere with the mean energy and energy flux of precipitating electrons have been developed, which are afterward introduced in the "standard" TIE-GCM code to calculate the conductivities. Validation is carried out, on the one hand, by comparing the resulting height-integrated conductivity distributions with the conductance model of *Marklund et al.* [1988] on occasion of magnetically disturbed conditions, and, on the other hand, by comparing observed ground magnetic perturbations with those output by the model.

2. AMPERE and TIE-GCM

2.1. The AMPERE Mission

The AMPERE satellite mission aims at providing global continuous observations of Birkeland currents with sufficient sampling cadence to chart global-scale dynamics [e.g., *Korth et al.*, 2010; *Anderson et al.*, 2014]. Its main scientific goal is to understand the coupled electrodynamic response of the ionosphere and magnetosphere to solar wind forcing. It is based on the constellation of the Iridium communications satellites, which consists of 66 active vehicles flying at an altitude of 780 km distributed over six circular polar orbit planes. Each space vehicle is equipped with a 30 nT resolution magnetometer, allowing the global radial current density to be estimated every 10 min by means of Ampère's law. Inversions are based on spherical harmonic fits to the global magnetometer data with degree 60 and order 5, implying a half-wavelength resolution of 3° in latitude and 36° in longitude. AMPERE data are available in the period from 1 January 2010 to 28 May 2013.

2.2. The TIE-GCM Model

The TIE-GCM is a comprehensive, first-principle model of the coupled thermosphere-ionosphere system that includes a self-consistent solution of the low-latitude electric field [*Roble et al.*, 1988; *Richmond et al.*, 1992]. The model solves the three-dimensional momentum, energy, and continuity equations for neutral and ion species at each time step using a centered finite difference scheme. Its outputs are numerous quantities relative to the upper atmosphere, such as density of electrons and different ion species, electric fields, conductivities, and currents, among many others.

The standard TIE-GCM makes use of an empirical electric potential model depending on the geospace conditions to drive the high-latitude ionospheric convection pattern. The global electric potential is then synthesized by combining the latter with the low-latitude dynamo potential. The process is summarized below.

The high-latitude electric potential in the standard TIE-GCM depends either on solar wind and interplanetary magnetic field (IMF) parameters or on geophysical indices such as Kp, which measures solar particle radiation by its ground magnetic effects. In this latter approach, Kp is used to parameterize both the high-latitude electric potential based on the empirical works of *Heelis et al.* [1982] and *Emery et al.* [2012], and the part of the ionospheric conductivity arising from particle precipitation. In particular, the conductivity is consistently calculated on the basis of an auroral precipitation model developed by *Roble and Ridley* [1987] that determines the mean energy and energy flux of the precipitating electrons, and an energy deposition code by *Roble and Rees* [1977]. Unlike the energy flux, which is allowed to vary with magnetic activity, the characteristic energy is not sensitive to the activity level in the standard version of the model, and it simply varies gradually in longitude from a tentative value of 1.5 keV in the dayside auroral oval and a constant value of 2 keV in its nightside.

The middle latitude and low-latitude electric potential Φ is calculated separately from the high-latitude one in the standard model. The starting points are the current continuity equation between the ionosphere and the magnetosphere, and Ohm's law for the current density in the ionosphere. Using the second equation into the first, assuming that Φ is constant along magnetic field lines, expressing all the quantities in terms of modified magnetic apex coordinates (which account for the nondipolar shape of the magnetic field), and integrating between the boundaries of the conducting ionosphere, one obtains the so-called electrodynamo equation [*Richmond*, 1995a]:

$$\frac{1}{R^2 \cos \lambda_m}\left[\frac{\partial}{\partial \varphi_m}\left(\frac{\Sigma_{\varphi\varphi}}{\cos \lambda_m}\frac{\partial \Phi}{\partial \varphi_m} + \Sigma_{\varphi\lambda}\frac{\partial \Phi}{\partial \lambda_m}\right) + \frac{\partial}{\partial \lambda_m}\left(\Sigma_{\lambda\varphi}\frac{\partial \Phi}{\partial \varphi_m} + \Sigma_{\lambda\lambda}\cos \lambda_m\frac{\partial \Phi}{\partial \lambda_m}\right)\right]$$
$$= \frac{1}{R \cos \lambda_m}\left[\frac{\partial K_{m\varphi}^D}{\partial \varphi_m} + \frac{\partial\left(K_{m\lambda}^D \cos \lambda_m\right)}{\partial \lambda_m}\right] + J_{mr}, \tag{1}$$

where λ_m and φ_m are the local modified magnetic apex coordinates; Σ_{ij} are the components of the conductance tensor in the direction represented by i, j; R can be taken as the radius of the base of the ionosphere; K_{mi}^D is the integrated dynamo or wind-driven current in the coordinate direction i; and J_{mr} is approximately the radial current at the top of the ionosphere.

The conductances (Σ_{ij}) and dynamo terms (K_{mi}^D) in (1) are self consistently calculated by the standard model essentially in terms of the $F_{10.7}$ radio flux (which is a proxy of the ionizing solar radiation) [*Solomon and Qian*, 2005] and with the help of a global-scale wave model [*Hagan and Forbes*, 2002, 2003] to specify the atmospheric tides in the low-altitude boundary. J_{mr} is not known, but at middle and low latitudes the field-aligned currents are assumed to be interhemispheric, meaning that all of the currents that exit the top of the ionosphere in one hemisphere follow the magnetic flux tubes and enter the conjugate ionosphere without gains or losses. In consequence, adding the electrodynamo equations for the two hemispheres, the field-aligned currents have opposite signs and cancel out, and an equation is left where the only unknown is the electric potential Φ. The resulting differential equation is then solved for Φ at middle and low latitudes, which, combined with that of high latitudes (as explained above), gives the global electric potential. Once Φ is known, together with the conductivities and the neutral winds, the global ionospheric electrodynamics is also determined.

2.3. The AMPERE-Driven TIE-GCM

The approach considered in this work and in *Marsal et al.* [2012] differs from the standard TIE-GCM in that geomagnetic field-aligned currents measured by the Iridium satellites are used in the model to feed the current continuity equation between the ionosphere and the magnetosphere; in particular, the AMPERE currents are basically used as J_{mr} in equation (1). This essentially allows calculating the global electric potential in the ionosphere at once, without distinction between high and low latitudes [see *Richmond and Maute*, 2013]. Together with the ionospheric conductivities, this allows to calculate the ionospheric current and its ground
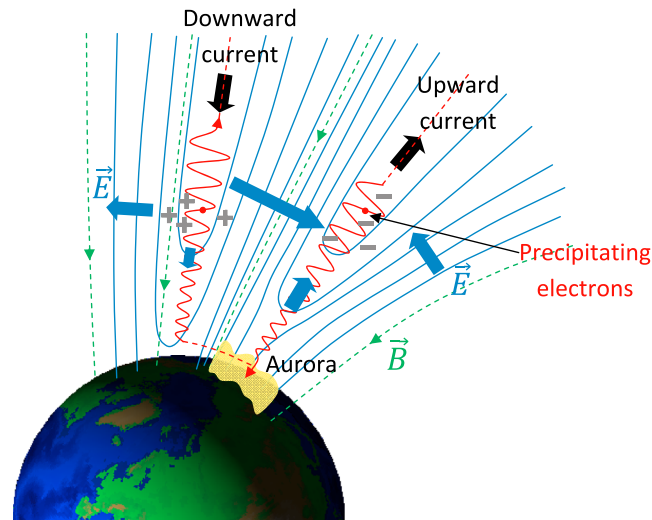
Figure 1. Sketch of the parallel electric fields above the auroral oval as the mechanism considered in this study to accelerate the electrons. Blue lines represent electrostatic potential contours, while green dashed lines represent magnetic field lines. Blue arrows show the electric field. Accelerated electrons (whose spiraling trajectories are represented with red lines) in the upward current region produce additional conductivity in the ionosphere, together with the discrete auroral display.

magnetic signature in an ensuing step, following the procedure described by *Richmond* [1974]. The theoretical basis of this approach is described in detail in *Marsal et al.* [2012], and an application is presented in the latter and in *Blanch et al.* [2013]. The use of the AMPERE currents to drive the TIE-GCM has shown to allow for a more direct, higher space-time resolution representation of the ionospheric electrodynamics.

3. Conductivities Consistent With Birkeland Currents (Theoretical Basis)

Marsal et al. [2012] used the Σ_{ij} and K_{mi}^D terms self consistently calculated by the standard TIE-GCM model in terms of Kp and $F_{10.7}$ in equation (1); however, use has been made here for the first time of conductivities consistent with the AMPERE field-aligned currents. Even though a general relationship with predictive power between Birkeland currents and conductances is not guaranteed at present due to the intrinsic complexity of the interplaying phenomena, the underlying idea is based on the well-known fact that ionospheric conductivities are enhanced where prominent upward Birkeland currents flow, i.e., where electrons are expected to precipitate after field-aligned acceleration. In this study, the acceleration mechanism is assumed to be produced by parallel electric fields (see sketch in Figure 1), thereby neglecting plasma wave fields, which otherwise might play a predominant role at localized regions such as the cusp and the polar cap boundary of the premidnight auroral oval [*Chaston et al.*, 2003]. Thus, the AMPERE field-aligned currents are not only used as a measure of J_{mr} in equation (1) but also this information is used to obtain a closer estimate of the ionospheric conductance tensor Σ_{ij} (also appearing in (1)) in the auroral zone. The procedure is explained in the following paragraphs, while tools are provided that allow being critical of the proposed method and the limits of its applicability.

The starting point is the specification of the aurora given by *Zhang and Paxton* [2008], who provide empirical formulations on the energy flux and mean energy of precipitating electrons at each point of the top of the ionosphere as a function of the Kp index, based on a number of global far ultraviolet observations made by the Global Ultraviolet Imager instrument mounted on the Thermosphere, Ionosphere, Mesosphere Energetics and Dynamics satellite [e.g., *Paxton et al.*, 2000]. The present approach consists in identifying *Zhang and Paxton's* [2008] specification with the base diffuse aurora in the TIE-GCM.

The specification of the discrete aurora, on the other hand, is based on the paper by *Knight* [1973], whose results have been confirmed by recent works [e.g., *Korth et al.*, 2014]. That author considers a magnetic field line from the high-latitude auroral zone to the magnetospheric neutral sheet along which the magnetic field strength decreases monotonically. A Maxwellian steady state solution for the electron distribution function is assumed to exist in the plasma sheet region, and the thermoelectric effect is considered with thermal plasmas at different temperatures at either end of the magnetic field line, i.e., the ionosphere and the plasma sheet. A monotonically decreasing potential difference is then added between these two ends. This allows the computation of the electron flux from one end to the other, which in turn gives rise to a theoretical value of the field-aligned current. In conclusion, the field-aligned current density is given as a function of the potential difference between the plasma sheet and the ionospheric ends of the field line. The given formulation also depends on the electron temperature, T, and the electron number density, N, at the two ends, as well

as on the ratio β of the magnetic field strength at the ionosphere (B_I) to plasma sheet (B_S) bases (i.e., $\beta \equiv B_I / B_S$), as expressed in the following equation:

$$J_\| = e\left\{ N_S \sqrt{\frac{kT_S}{2\pi m_e}} \left[\beta - (\beta-1)e^{-\frac{eV}{kT_S}\frac{1}{\beta-1}} \right] - N_I \sqrt{\frac{kT_I}{2\pi m_e}} \left[\beta - (\beta-1)e^{-\frac{eV}{kT_I}\frac{1}{\beta-1}} \right] e^{-\frac{eV}{kT_I}} \right\}, \tag{2}$$

where $J_\|$ is the resulting upward field-aligned current at the top of the ionosphere, e (in *italics*) is the elementary charge or minus the electron charge, m_e the electron mass, k the Boltzmann constant, and $V = \Phi_I - \Phi_S$ the potential difference between the ionosphere and the plasma sheet bases (note that negative potential drops are not treated in *Knight's* [1973] theory). The subscripts S and I in the state parameters denote the plasma sheet and ionosphere bases, respectively.

Since the current is assumed to be primarily carried by electrons, it is useful to think of the first term on the right-hand side within the braces of (2) as the downward flux of electrons precipitating from the plasma sheet region, F_S, and the second term as the upward flux of electrons from the ionosphere, F_I, so that $J_\| = e(F_S - F_I)$. Let us define

$$F_0 \equiv N_S \sqrt{\frac{kT_S}{2\pi m_e}} \tag{3}$$

the downward flux of electrons from the plasma sheet for a zero potential drop, i.e., essentially the number density times the thermal velocity of the plasma sheet electron population. It should be pointed out that such electron flux, though it has not been accelerated by parallel electric fields, is still capable of producing certain ionization upon incidence onto the auroral ionosphere. This flux is deemed responsible for the diffuse aurora and is quantified in the present work by the *Zhang and Paxton* [2008] formulation. It can be checked from (2) that F_S increases monotonically from a value of F_0 (for no potential difference) up to a value of βF_0 for an infinite potential drop. The flux F_I, on the contrary, is considered not to produce effective ionization. Although the cases when $V < 0$ are not contemplated in Knight's theory, satellite observations [*Cattell et al.*, 2004] show that for a given amplitude of the downward field-aligned current, the potential drop is observed to be a fraction of that observed in upward field-aligned currents of the same amplitude (see an application in *Wiltberger et al.* [2009]). Consistent with this fact, V is considered to be close to zero for any downward parallel current, which implies $F_S = F_0$.

The plasma sheet electron temperature, T_S, is of the order of several 10^6 K, while that of the ionosphere base is just a few 10^3 K, so $T_S/T_I \sim 10^3$. The case of the electron densities is opposite: while N_S is of the order of 10^5 to 10^6 m^{-3}, N_I depends on the exact height being considered, but it is about 6 orders of magnitude higher. Finally, given that the magnetic field in the high-latitude ionosphere $B_I \sim 5 \times 10^4$ nT and that of the plasma sheet $B_S \sim 10$ nT, $\beta \equiv B_I / B_S$ may be as large as 5000. However, if the acceleration process takes place about 1 R_E above the ionosphere, β may be as low as 10 [*Fridman and Lemaire*, 1980].

The TIE-GCM essentially requires the number flux F_S and the mean energy $\bar{E}$ of the precipitating electrons to compute the auroral conductivities from the deposition code. Thus, in the following discussion, an expression is pursued for these quantities as a function of the field-aligned current (i.e., the AMPERE) input.

From (2) and (3), it is straightforward to see that $F_S = F_0$ is a very good approximation when $eV \le 0.05 kT_S$. On the other hand, from the above discussion about the typical values of the state parameters at the two ends of the field line, it follows that $F_I = 0$ results in an excellent approximation when $eV > 0.05 kT_S$, which implies $J_\| = eF_S$. Since $F_S \ge F_0$ and $F_S \ge J_\|/e$ (i.e., the flux of downgoing electrons must be greater or at least equal to the net downward flux), it turns out that $J_\|/e > F_0$ implies $eV > 0.05 kT_S$, and therefore $F_S = J_\|/e$; otherwise (i.e., when $J_\|/e \le F_0$) $F_S = F_0$ is employed. Using the AMPERE satellite measurements to compute $J_\|$, this provides the number flux of electrons.

On the other hand, the mean energy of the precipitating electrons at each point of the ionosphere base is defined as

$$\bar{E} = \frac{\int_{E_k=0}^{\infty} E_k dF_S(E_k)}{\int_{E_k=0}^{\infty} dF_S(E_k)} = \frac{\int_{E_k=0}^{\infty} E_k f_S(E_k) dE_k}{\int_{E_k=0}^{\infty} f_S(E_k) dE_k} = \frac{Q}{F_S}, \tag{4}$$

where E_k is the kinetic energy (normally expressed in keV units in the literature) of the electrons from the source region; dF_S (typically 1/cm^2/s) is the differential flux of electrons with kinetic energies within a differential energy interval dE_k; $f_S(E_k) \equiv dF_S/dE_k$ (1/cm^2/s/keV) is the number flux density; and Q (usually erg/cm^2/s) is the associated
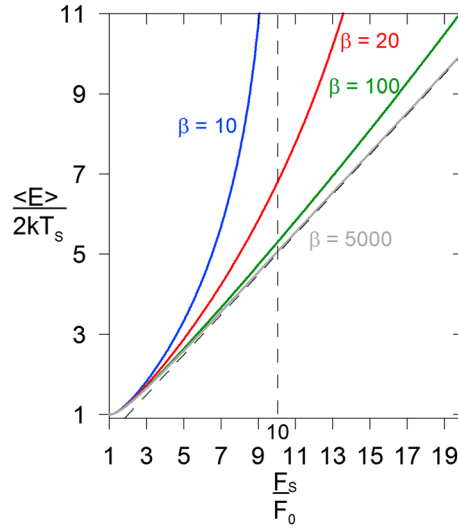
Figure 2. Mean energy in the ionosphere base as a function of the flux of precipitating electrons (both relative to their purely Maxwellian values) for various β values.

overall energy flux. Note that the above quantities are evaluated at each point of the surface defined by the top of the high-latitude ionosphere.

Let us assume a purely Maxwellian distribution function in the electron source region, though it is known that the real form is that of a kappa distribution, that is, Maxwellian, but with a power law tail at high energies [*Newell et al.*, 2009]. This election is justified by *Robinson et al.* [1987], who show that the conductances produced by Maxwellian electron distributions are good approximations to those produced by arbitrary distributions, provided the arbitrary spectra are compared to Maxwellians with the same average energy. The number flux density in the magnetosphere, in this case, is proportional to $E_k \exp(-E_k/kT_S)$.

When there is no potential drop between the magnetosphere and the ionosphere bases, the expression for the flux density is transferred to the ionosphere unchanged, so $f_s(E_k)$ is also proportional to $E_k \exp(-E_k/kT_S)$. Using this expression in equation (4) yields a mean energy equal to $2kT_S$. Introducing a potential drop V in the Maxwellian, however, produces a change in the auroral spectrum measured in the ionosphere. Perhaps, the most immediate change is that there can be no electrons with energies below eV. Even in this case, however, it is still possible to find an exact expression for $\bar{E}$ from (4) (see equation (A18) in Appendix A):

$$\bar{E} = 2kT_S + \frac{eV}{1 + \frac{1}{\beta}\left(e^{\frac{eV}{kT_S}\frac{1}{\beta-1}} - 1\right)^{-1}}, \tag{5}$$

which reduces to $2kT_S + eV/(1 + kT_S/eV)$ for the common case when $eV/kT_S \ll \beta$ or to $kT_S + eV$ when additionally $eV/kT_S \gg 1$.

Expressing eV as a function of F_S based on (2), one obtains

$$eV = kT_S(\beta - 1)\ln\left(\frac{\beta - 1}{\beta - \frac{F_S}{F_0}}\right),$$

from which one gets the sought expression for the mean energy (5) as a function of the precipitating electron flux or, equivalently, as a function of the field-aligned current:

$$\bar{E} = 2kT_S\left[1 + \frac{\beta}{2}\left(1 - \frac{F_0}{F_S}\right)\ln\left(\frac{\beta - 1}{\beta - \frac{F_S}{F_0}}\right)\right]. \tag{6}$$

$\bar{E}$ reduces to $kT_S(F_S/F_0 + F_0/F_S)$ for the common case when $F_S/F_0 \ll \beta$ or to $kT_S F_S/F_0$ when additionally $F_S/F_0 \gg 1$. Based on equation (6), Figure 2 illustrates the dependence of the mean energy (normalized to its Maxwellian value) on the ratio of the accelerated (F_S) to nonaccelerated (F_0, or purely Maxwellian) flux.

As said above, the *Zhang and Paxton* [2008] mean energy and number flux density are identified with $2kT_S$ and F_0, respectively, so from (4) it follows that $F_0 = Q_{ZP}/\bar{E}_{ZP}$. The number flux F_S, the energy flux Q, and the characteristic energy α, which is half the mean energy $\bar{E}$, are the three quantities used in the TIE-GCM to specify the aurora. In the present approach, these input quantities are obtained following the procedure summarized in Table 1, where the notation $J_\parallel$ has been replaced with $J_\parallel^{AMP}$ to emphasize the use of the AMPERE data set as an input. From Table 1, it is seen that F_S takes the value $Q_{ZP}/\bar{E}_{ZP}$ when $J_\parallel^{AMP} \leq eQ_{ZP}/\bar{E}_{ZP}$, and $J_\parallel^{AMP}/e$ otherwise. In this sense, the quantity $eQ_{ZP}/\bar{E}_{ZP}$ is referred to as the Zhang-Paxton threshold. The advantage of

Table 1. Approach Used to Obtain the Flux F_S and the Characteristic Energy α to be Input in the TIE-GCM[a]

	F_S	$\alpha\ (=\bar{E}/2)$
$J_\parallel^{AMP} \leq \dfrac{eQ_{ZP}}{\bar{E}_{ZP}}$	$\dfrac{Q_{ZP}}{\bar{E}_{ZP}}$	$\dfrac{\bar{E}_{ZP}}{2}$
$J_\parallel^{AMP} > \dfrac{eQ_{ZP}}{\bar{E}_{ZP}}$	$\dfrac{J_\parallel^{AMP}}{e}$	$\dfrac{\bar{E}_{ZP}}{2}\left[1 + \dfrac{\beta}{2}\left(1 - \dfrac{eQ_{ZP}}{J_\parallel^{AMP}\bar{E}_{ZP}}\right)\ln\left(\dfrac{\beta-1}{\beta - \dfrac{J_\parallel^{AMP}\bar{E}_{ZP}}{eQ_{ZP}}}\right)\right]$

[a]The superscript "AMP" stems from AMPERE; the subscript "ZP" refers to the *Kp*-dependent functions specified by *Zhang and Paxton* [2008].

identifying the *Zhang and Paxton* [2008] specification with the diffuse aurora is that the values of the state parameters (i.e., temperatures and densities) at the ionosphere and electron source regions are no longer needed, but these values are implicit in that specification as a function of *Kp*. The energy flux Q is obtained as the product $\bar{E}F_S$ ($=2\alpha F_S$) from (4).

The quantity β in Table 1 is calculated at each latitude as the ratio B_I/B_S, where B_S is calculated as a function of the distance to the point that the corresponding field line crosses the dipole equator. This approximation, indeed, often constitutes a lower limit for β, as the International Geomagnetic Reference Field (IGRF) model is used to trace the field line to the equator, whereas real field lines are elongated toward the magnetotail. Tests have been carried out with different lower values of β during disturbed conditions, regarding the possibility that the source region may be closer to the Earth during these occasions. However, the quantities output by the TIE-GCM show little sensitivity to this parameter.

It is also known that sunlight, and in general higher conductivity regions previously present in the ionosphere, suppresses the discrete aurora [e.g., *Blomberg and Marklund*, 1988; *Newell et al.*, 1996; *Wiltberger et al.*, 2009]. This effect has also been simulated in the present model by an effective reduction of the parallel currents on the dayside auroral oval, where the extreme ultraviolet conductance is relatively high. As in the work by *Wiltberger et al.* [2009], the energy of the precipitating electrons in the auroral zone has been set inversely proportional to the EUV-induced Pedersen conductance Σ_P^{EUV}, which in turn is a function of the solar zenith angle χ [*Richmond*, 1995b]. The formula that has been adopted here for the effective field-aligned current for purposes of calculating the ionospheric conductance is

$$J_{\parallel\ eff}^{AMP} = \begin{cases} J_\parallel^{AMP}\dfrac{\Sigma_P^{EUV}(80°)}{\Sigma_P^{EUV}(\chi)} = J_\parallel^{AMP}\sqrt{\dfrac{\cos 80°}{\cos \chi}} & \chi < 80° \\ J_\parallel^{AMP} & \chi \geq 80° \end{cases}$$

resulting, e.g., in an effective 36% reduction of $J_\parallel^{AMP}$ for a solar zenith angle of 65°, while the parallel current remains unchanged above 80° (e.g., in the night sector).

Note that the *Zhang and Paxton* [2008] formulation on the energy flux and mean energy of precipitating electrons as a function of *Kp* is a statistical mean based on a number of satellite passes for a given value of *Kp*. This average contains not only diffuse but also discrete precipitation regions, especially as *Kp* increases and at the upward region 1 (R1) current sector [*Korth et al.*, 2014]. This means that the values of $\bar{E}$ (and so α) and $Q = \bar{E}F_S$ being used are indeed somewhat overestimated. To avoid this, the following step consists in adjusting the initial guesses for F_0 and $\bar{E}_{ZP}$ that are given in the upper row of Table 1 so that the two following conditions are simultaneously met: (a) the hemispheric average of the mean energy for each *Kp* equals the empirical *Kp*-dependent hemispheric average of $\bar{E}$ given by *Zhang and Paxton* [2008]; and (b) the Hemispheric Power (HP), which is the hemispherically integrated energy flux, equals their empirical *Kp*-dependent HP. This is an iterative process that converges to mean energies and fluxes more according to observations. In practice, however, the final values of F_0 and $\bar{E}_{ZP}$ are usually within 10% of the initial guess, indicating that the original values were sufficiently good.

The overall result of the present approach is an auroral specification that gives more weight to enhanced upward currents (as given by the AMPERE data set) with respect to the empirical *Zhang and Paxton's* [2008] mean auroral specification for a given *Kp*. The values of the number and energy flux thus obtained are introduced in the energy deposition code of the standard TIE-GCM, from which the conductivities are calculated.

Table 2. Geodetic and Quasi-Dipole Coordinates (for the Epoch 2013.0) of Geomagnetic Observatories[a]

	Geodetic Longitude	Geodetic Latitude	QD Longitude	QD Latitude
Tromsø (TRO)	18.9	69.7	101.9	66.7
College (CMO)	212.1	64.9	266.8	65.0
Ebre (EBR)	0.5	40.8	76.6	34.6
Livingston Island (LIV)	299.6	−62.7	11.2	−48.6

[a]Units are in degrees (positive eastward and northward). QD, quasi-dipole.

4. Model Application

This section includes results and discussion relative to several case studies the AMPERE-driven TIE-GCM (with conductivities consistent with Birkeland currents) has been applied to. In particular, the ground magnetic perturbations of the resulting ionospheric currents are compared with contemporaneous observations at different sites and for different magnetic disturbance levels. The ionospheric conductances yielded by the model have also been put side by side with an existing model that accounts for precipitation-induced conductance enhancements. Comparisons with the standard TIE-GCM and with the results of *Marsal et al.* [2012] have also been carried out to evaluate the impact of the present modification.

4.1. Model Validation Tools

In order to evaluate how well the modeled ground magnetic perturbations fit the observations, the performance (*P*) parameter is introduced [see *Torta et al.*, 2014]:

$$P = 100\left(1 - \frac{\text{RMSD}_{om}}{\sigma_o}\right), \tag{7}$$

where σ_o is the standard deviation of the set of observations for a given case study, and RMSD_{om} the root-mean-square deviation of the residuals (or differences between model and observations). One can think of *P* as the (percentual) fraction of the standard deviation of the observations which can be explained by the model.

Note that the TIE-GCM is essentially meant to give the magnetic contribution arising from the currents flowing in the ionosphere and a simplified system of closing field-aligned currents, no account being made of important currents such as those developed in the magnetosphere during disturbed conditions (precisely those we are most interested in), not to mention the slowly varying core and crustal fields. Indeed, it also includes a simplified ground conductivity model consisting of a sphere of perfectly conducting material below a certain depth (see section 4.2) and a perfect insulator above, thus neglecting the real 3-D variation. This implies that the maximum value of *P* is not expected to be 100% in any case but rather around 80% at high latitudes during disturbed conditions (where the weight of ionospheric currents is relatively high), going down to 75–70% at middle and lower latitudes (where the weight of the magnetopause and ring current systems is expected to dominate) [see, e.g., *Olsen*, 1996].

Another means to evaluate the present model, and in particular the approach of conductivities consistent with field-aligned currents, is provided by comparing the conductances with another previous work in which auroral electron precipitation was accounted for. Specifically, the output will be compared with the results arising from the application of the expressions given by *Marklund et al.* [1988]. In that and other related works [e.g., *Blomberg and Marklund*, 1988, 1991], the authors propose a linear relationship between the conductance enhancements and the upward field-aligned currents. As in the present case, the proportionality factors, *k*, are functions of magnetic local time (MLT), reaching a minimum during daytime, thus accounting for the differences in the hardness of the particle spectrum. However, despite the remarkable differences in solar illumination, *k* does not depend on the season within the year, the summer solstice being treated as the winter one. Using the AMPERE currents as an input to the *Marklund et al.* [1988] model, a conductance distribution is obtained that is compared with the one output by the AMPERE-driven TIE-GCM. Because of the approximations assumed by *Marklund et al.* [1988], i.e., linearity between $J_\parallel$ and conductance, and simple MLT dependence of *k*, a close matching of the two conductance distributions is not expected but rather an order-of-magnitude impression on the compatibility of these two methods. A more direct validation would be attained by instantaneous observations of Birkeland currents and conductances. The most accurate estimates of this quantity correspond to incoherent scatter radar (ISR) measurements combined with a neutral atmosphere model. In this sense, it is worth noting that the present study cannot be strictly taken as a proper benchmark of the model applicability.
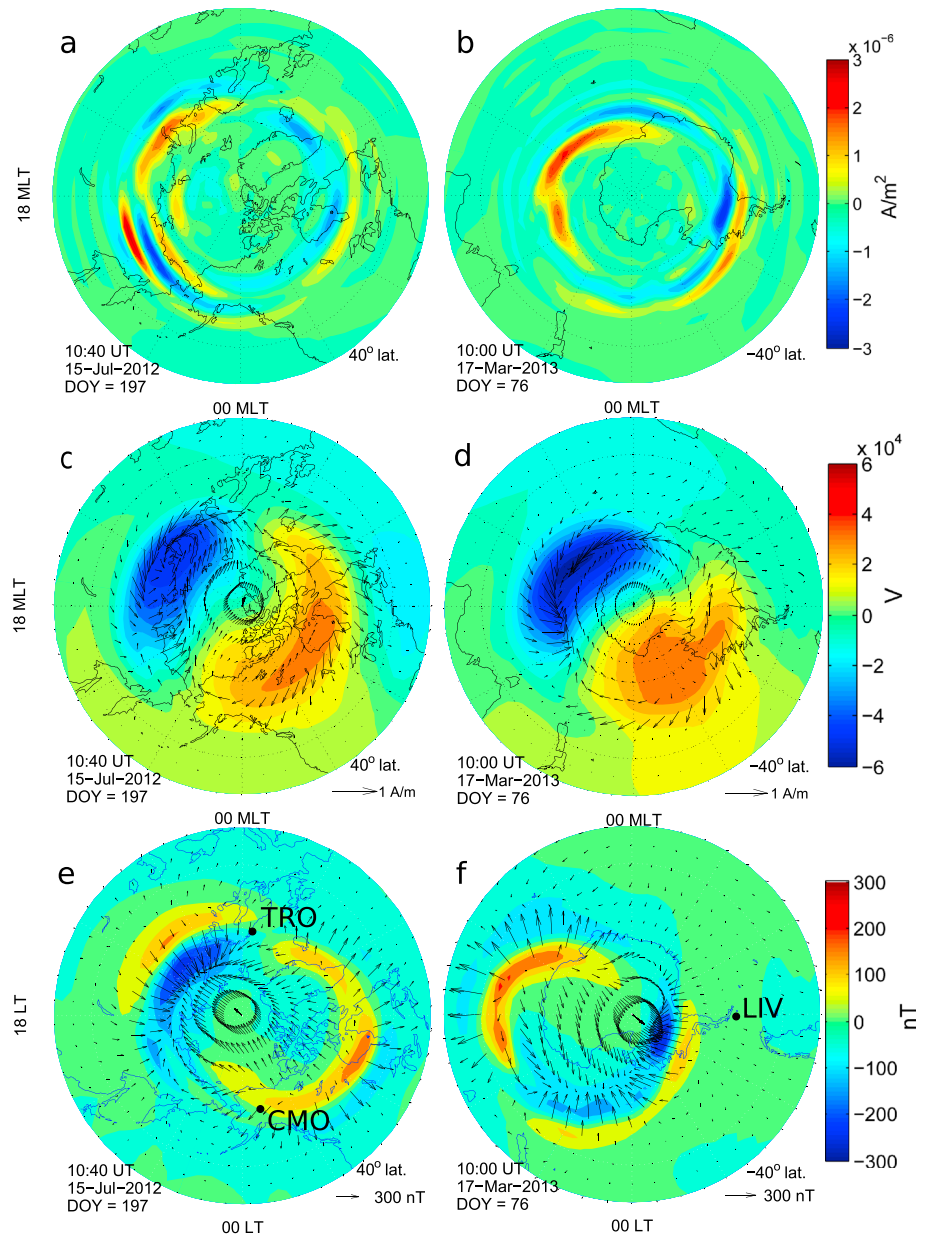
Figure 3. Azimuthal equidistant projection maps showing different electrodynamic quantities at given disturbed instants. (a and b) The AMPERE field-aligned currents (A/m^2; positive upward) used as an input to the TIE-GCM; (c and d) the output electric potential (V) around 100 km height with superposed height-integrated horizontal current vectors (A/m; see scale at the bottom right corner); and (e and f) the output ground magnetic perturbations (nT). Arrows in Figures 3e and 3f correspond to the horizontal projection of the vector magnetic perturbations (see scale at the bottom right corner), while contour lines correspond to the vertical component (positive downward). QD coordinates are used in Figures 3a–3d while geodetic in Figures 3e and 3f. Figures 3a, 3c, and 3e correspond to the conditions on 15 July 2012 at 10:40 UT, and Figures 3b, 3d, and 3f to those on 17 March 2013 at 10:00 UT. The locations of TRO, CMO, and LIV magnetic observatories are indicated in Figures 3e and 3f.

4.2. Results

Given that the AMPERE field-aligned current input makes the greatest difference with respect to the standard TIE-GCM during disturbed conditions, and because the most affected (magnetic) latitudes are essentially those between 63° and 70°, the present model is expected to yield comparatively better results for gradually more disturbed conditions and increasing latitudes. For this reason, the modified TIE-GCM has been run for five periods between 2010 and 2013 in which AMPERE data are available, ranging from moderate to highly disturbed conditions. As for the geomagnetic observatories chosen to validate the model, two of them (Tromsø (TRO) and College
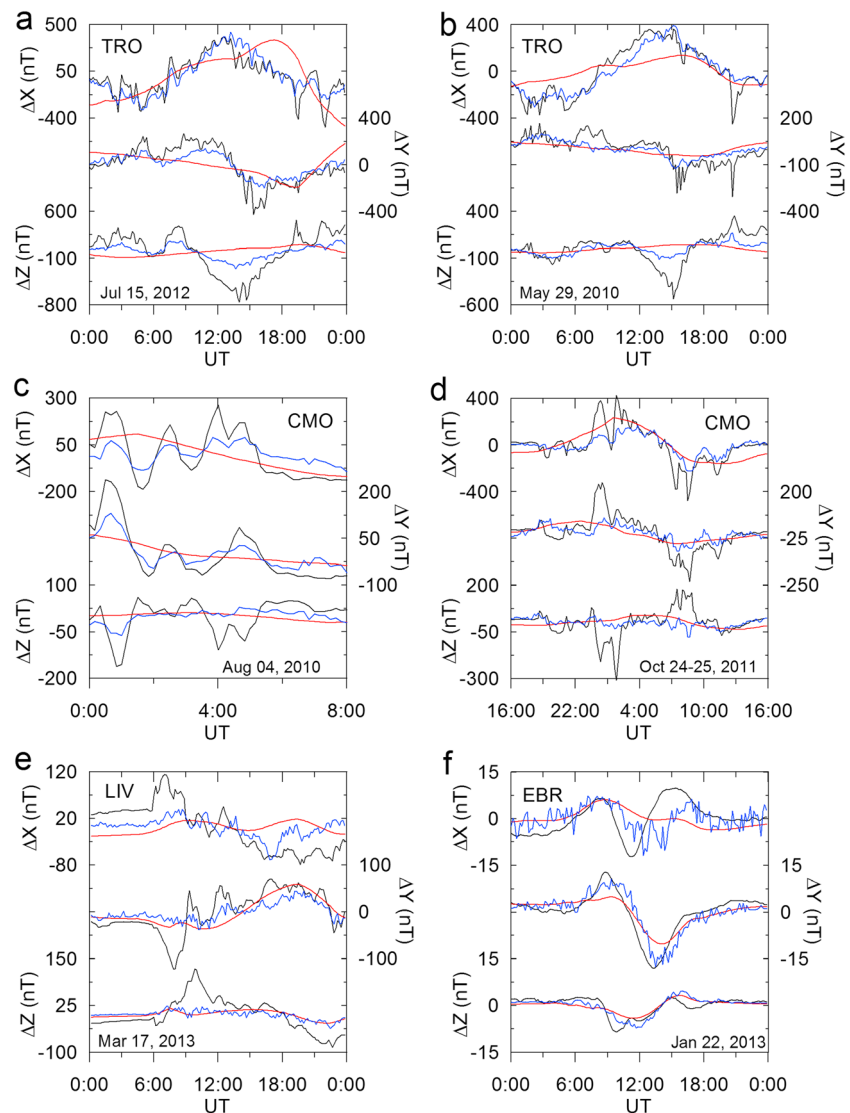
Figure 4. Ground magnetic perturbations versus time at the location of the observatories used to validate the model. The upper, middle, and lower subplots of each panel correspond to the X, Y, and Z components of the magnetic variations, respectively. The black line corresponds to the observed variation at the observatory in question, while the red and blue lines represent the standard and AMPERE-driven versions of the TIE-GCM, respectively. The periods displayed correspond to the most disturbed interval (the least in the case of the quiet period, Figure 4f). Note that the average has been subtracted to each curve so as to make them comparable.

(CMO)) are close to or within the auroral zone. However, in order to evaluate how the model works in different conditions, two midlatitude observatories (Ebre (EBR) and Livingston Island (LIV)) and a completely quiet period have also been included. Table 2 summarizes the observatory locations, while the selected periods, along with the Ap index as a measure of their disturbance level, can be found in the header of Table 3.

Figure 3 presents azimuthal equidistant projection maps showing different quantities corresponding to selected instants of the above periods. Figures 3a, 3c, and 3e correspond to the conditions present on 15 July 2012 at 10:40 UT; Figures 3b, 3d, and 3f correspond to those on 17 March 2013 at 10:00 UT. Figures 3a and 3b show the AMPERE field-aligned currents used as an input to the model; Figures 3c and 3d show the electrostatic potential output by the model, with superposed height-integrated horizontal ionospheric current vectors; and Figures 3e and 3f show the output ground magnetic perturbations. Note the prominent currents developed during such disturbed conditions at the edges of the potential extrema (Figures 3c and 3d), corresponding to the auroral electrojet, and the associated strong ground magnetic signatures (Figures 3e and 3f).

Table 3. Model Performance P Used as a Validation Means[a,b]

Obs.	Comp.	15 July 2012 (78[c]) A1	A2	17 March 2013 (72) A1	A2	24–25[d] October 2011 (60) A1	A2	4 August 2010 (49) A1	A2	29 May 2010 (28) A1	A2	22 January 2013 (1) A1	A2
TRO	P_X	**54**	**48**	*32*	*35*	*28*	*34*	*37*	*46*	*60*	*61*	*−272*	*−144*
	P_Y	*47*	*48*	*13*	*16*	*10*	*10*	*34*	*39*	*31*	*31*	*−106*	*−36*
	P_Z	*27*	*30*	*9*	*17*	*19*	*26*	*8*	*12*	*25*	*26*	*−137*	*−25*
CMO	P_X	*36*	*43*	*31*	*36*	**43**	**37**	**42**	**31**	*41*	*46*	*−172*	*−100*
	P_Y	*37*	*40*	*16*	*19*	*20*	*29*	*46*	*49*	*21*	*26*	*−44*	*−18*
	P_Z	*15*	*16*	*10*	*12*	*−6*	*−3*	*9*	*12*	**3**	**2**	*−61*	*−2*
LIV	P_X	**8**	**7**	**24**	**20**	*−5*	*−1*	**26**	**23**	**26**	**23**	*3*	*11*
	P_Y	*21*	*34*	*25*	*26*	*32*	*33*	**41**	**37**	**36**	**34**	**49**	**48**
	P_Z	*22*	*24*	*16*	*17*	*41*	*42*	**3**	**0**	*18*	*18*	**24**	**15**
EBR	P_X	*3*	*11*	**18**	**17**	*−12*	*−9*	*−4*	*−3*	*8*	*17*	*4*	*−8*
	P_Y	*31*	*35*	**2**	**0**	*26*	*32*	*13*	*13*	**23**	**13**	*43*	*49*
	P_Z	*16*	*16*	*13*	*13*	*−11*	*−9*	*3*	*4*	**14**	**10**	*27*	*39*

[a]A1 stems from the basic AMPERE-driven model; A2 from the present approach.
[b]Values in *italic* script denote improvement of the AMPERE-driven model with respect to the standard version; **boldface** indicates worsening.
[c]Parenthetical values correspond to the *Ap* index of the analyzed periods given in the usual 2 nT units.
[d]*P* and *Ap* values in this case are given for a 24 h period starting on 24 October 2011 at 16:00 UT.

Figure 4 shows plots of the ground magnetic perturbations at the location of the four observatories used to validate the model (see Table 2) for the six analyzed periods. Note that magnetic variations are plotted with respect to the mean. Figures 4a and 4b, 4c and 4d, and 4e and 4f correspond to the *X* or north component, *Y* or east component, and *Z* or vertical component, respectively. The black line represents the observed variations at the observatory in question, while the red and blue lines represent the output of the standard and AMPERE-driven versions of the TIE-GCM, respectively. The standard model is run using the *Heelis et al.* [1982] mode for the computation of the high-latitude potential (see section 2.2).

Recall that the main magnetospheric contribution is not accounted for in the model, thus an improved comparison between ground magnetic model and observations could be attained by adding the ring current effect to the model or, conversely, by removing its signature from the observations. This could be effected in the first approach by direct use of the *Dst* index or, more accurately, by a magnetic field model accounting for external contributions [e.g., *Maus et al.*, 2010; *Finlay et al.*, 2015; *Sabaka et al.*, 2015].

It is worth to note that the magnetic perturbations obtained by our first approach [*Marsal et al.*, 2012] are not significantly different from those produced by the present model, so they have not been included in the figure. It may also be worth to make an aside here in connection with the results presented by *Marsal et al.* [2012]. In particular, that article assayed with the so-called "NS, NH, and SH solutions" and with the depth of the perfect conducting layer to run the TIE-GCM. However, since the differences among these solutions are not significant, and because this discussion does not contribute substantial concepts in the present work, the NH solution has now been chosen throughout in Northern Hemisphere observatories, and the SH solution otherwise. Likewise, a fixed value of 250 km has been used for the depth of the conducting layer at the two high-latitude observatories, and a depth of 600 km at the two midlatitude stations.

Table 3 shows the model performance P (equation (7)) applied to the results of *Marsal et al.* [2012] (columns labeled "A1") and to the present approach (columns labeled "A2") for each of the 24 (= 6 periods × 4 observatories) cases analyzed. Note that P actually has three components, one for each component of the magnetic variation vector, i.e., P_X, P_Y, and P_Z. Italic and boldface scripts in Table 3 help identify improvement or worsening, respectively, of the present approach with respect to the results of *Marsal et al.* [2012]. It can easily be checked that improvement dominates throughout the table.

Figure 5 presents a subset of maps showing electrodynamic quantities relative to the auroral zone during the disturbed conditions present in 29 May 2010 at 10:20 UT. Figures 5b through 5d show the auroral zone Hall conductance distribution using different approaches. In particular, Figure 5b is the output obtained by the standard version of the model, which indeed is the conductance model used in our first approach; Figure 5c corresponds to the present approach, i.e., conductivities consistent with the AMPERE field-aligned
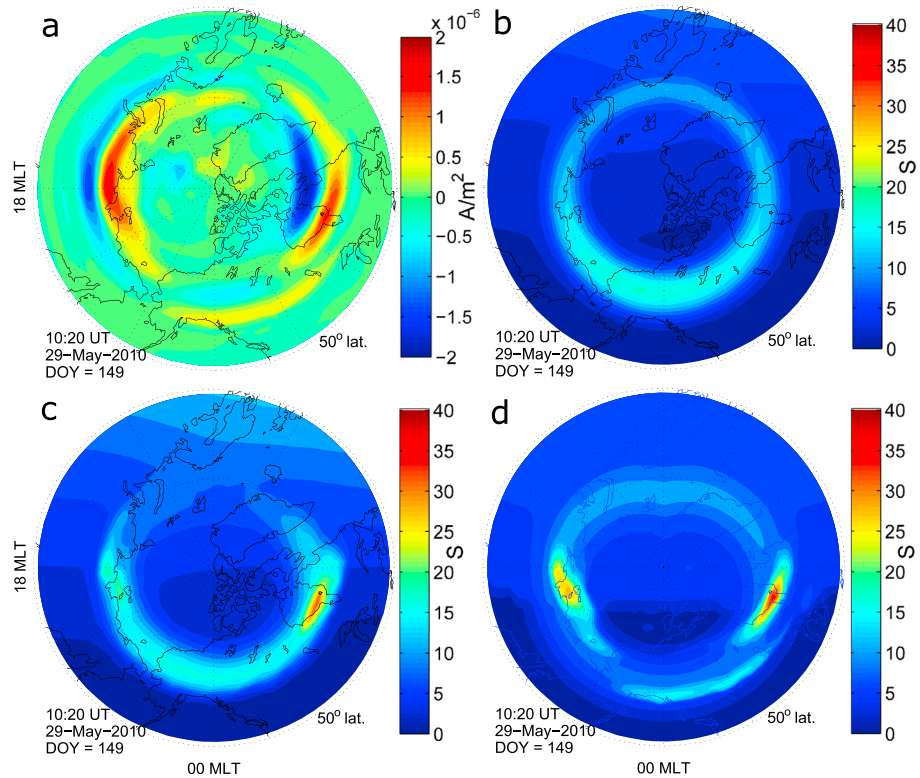
Figure 5. Set of electrodynamic quantities relative to the conditions occurring on 29 May 2010 at 10:20 UT. (a) input AMPERE field-aligned currents (A/m^2; positive upward); (b) Hall conductance (S) yielded by the standard TIE-GCM; (c) the TIE-GCM using conductivities consistent with field-aligned currents; and (d) the *Marklund et al.* [1988] model. Note the conductance enhancement in the predawn and dusk sectors of the auroral oval in Figures 5c and 5d. QD coordinates are used.

currents shown in Figure 5a; and Figure 5d is obtained using the model of *Marklund et al.* [1988]. For comparison purposes, a tentative value has been included to account for the EUV-induced conductivity, as well as for the diffuse and background precipitation in Figure 5d.

Other examples are presented in Figure 6, where a and b show the instantaneous distribution of the input AMPERE currents, c and d show the conductance output by the present model, and e and f show the same quantity output by the *Marklund et al.* [1988] model. Figures 6a, 6c, and 6e correspond to the disturbed conditions occurring on 4 August 2010 at 13:20 UT, while 6b, 6d, and 6f correspond to those on 24 October 2011 at 19:00 UT. Figures 6c and 6e for August 2010 represent Hall conductances, while 6d and 6f for October 2011 represent Pedersen conductances.

4.3. Discussion

The standard TIE-GCM (red lines in Figure 4) is observed to reproduce, to a certain extent, the slow variations of the magnetic field, especially during the highly disturbed conditions of Figure 4d. However, magnetic variations with periods shorter than 6–8 h are not reproduced. This is also the most notable difference with respect to the AMPERE-driven model and can be explained by the use of indices with a low temporal resolution in the standard version, like Kp or the $F_{10.7}$ solar flux, from which the magnetospheric conditions are updated with a maximum frequency of 3 h (at least for the Heelis mode) compared with the 10 min resolution of the AMPERE-driven version.

A mean performance value P of 17% is obtained by averaging the results of the present approach in Table 3 (columns with header A2), compared to a 9% for our first approach (header A1), and an 8% for the standard model (not shown). However, in general, both AMPERE-driven models perform better at high latitudes during high disturbance levels than at midlatitudes during quiet periods. Thus, if only the two high-latitude observatories and the five disturbed periods are considered (indeed, these are the situations we are most
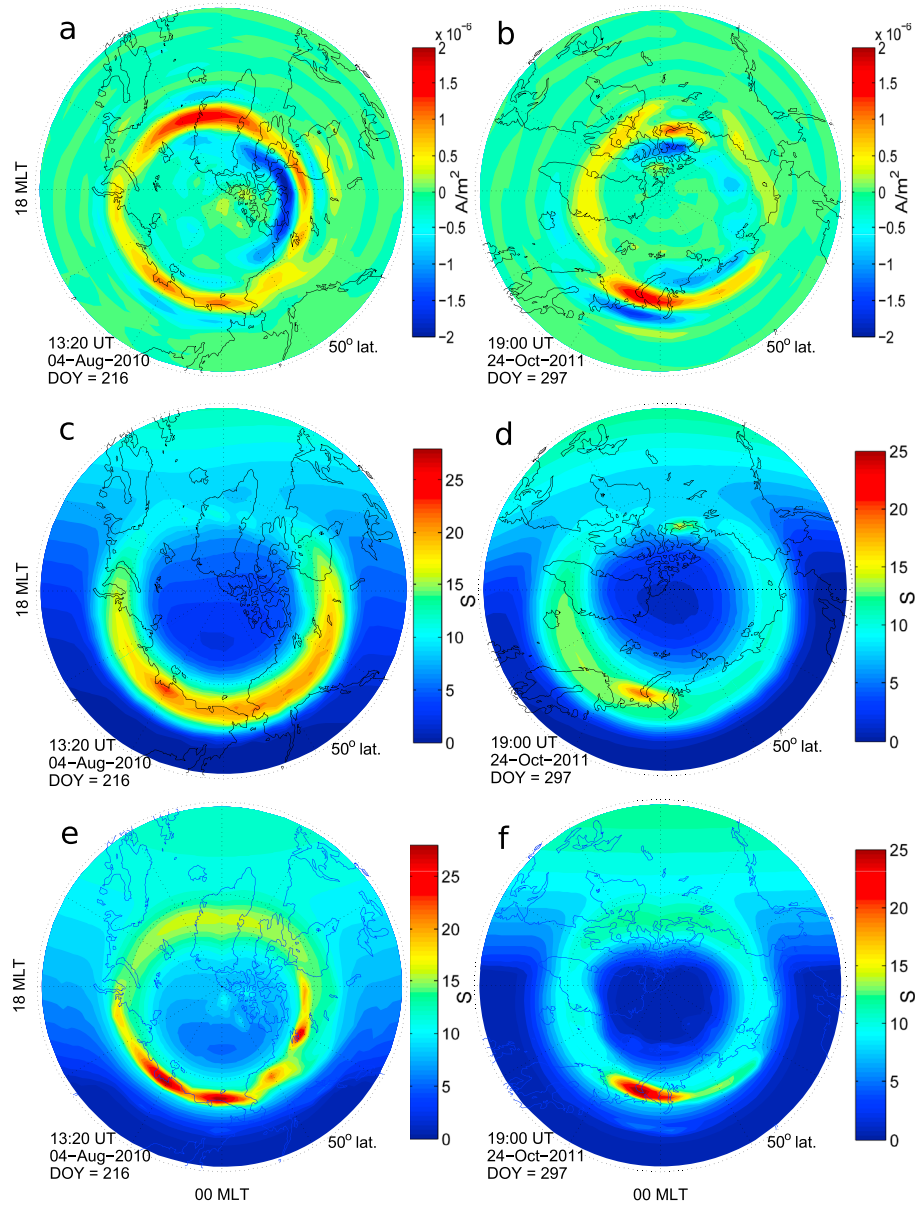
Figure 6. Set of electrodynamic quantities relative to the conditions occurring on (a, c, and e) 4 August 2010 at 13:20 UT and on (b, d, and f) 24 October 2011 at 19:00 UT. Figures 6a and 6b show the input AMPERE field-aligned currents (A/m^2; positive upward); Figures 6c and 6e show the Hall conductance (S) associated with field-aligned currents yielded by the present model and that of *Marklund et al.* [1988], respectively; Figures 6d and 6f show the Pedersen conductance (S) yielded by the present model and that of *Marklund et al.* [1988], respectively. Note the conductance enhancement in the premidnight sectors, consistent with enhanced upward currents. QD coordinates are used.

interested in), the performance of the present model rises to 29% versus a 26% for our first approach and a 5% for the standard model. As pointed out above, this improvement is due to the fact that the AMPERE currents used to drive the model play a more important role at auroral latitudes during disturbed conditions.

The quality of the high-latitude modeling is also substantiated in Figures 4a and 4b, where magnetic bays are reproduced to a great extent, and in 4c and 4d in a lesser degree. However, as in our previous papers [*Marsal et al.*, 2012; *Blanch et al.*, 2013], magnetic variations are still underestimated in this work even at high latitudes. One of the reasons pointed out in *Marsal et al.* [2012] was the lack of sensitivity of the model conductivity to ionization structures produced by precipitating electrons linked to upward AMPERE field-

aligned currents, and this is precisely what this work is concerned with. However, it can be seen that the improvement of the magnetic results by this fact is rather modest, amounting to an average 8% (9% versus 17%) increase in the performance parameter P. Unexpectedly, restricting the analysis to disturbed periods and high latitudes, the improvement reduces to just 3% (26% versus 29%).

As for quiet-time currents, uncertainties in model parameters and inputs like atmospheric tides prevent a better agreement. The noisy appearance of the present model (blue lines) in Figure 4f is a common feature of quiet periods, and it was also observed in *Marsal et al*. [2012].

The horizontal components of the magnetic variations, and in particular the X component, are better reproduced than the Z component. This applies to both the standard and the AMPERE-driven versions and is especially clear in Figures 4c–4e. Restricting the analysis to high latitudes and disturbed conditions, the average values of the model performance P for the X, Y, and Z components are 42%, 31%, and 15%, respectively (as deduced from Table 3; columns A2). The reasons for this defect in the vertical component may be diverse. On the one hand, combining the strong horizontal gradients of this component at high latitudes with inaccuracies arising from the limited resolution of AMPERE data, which is about 3° in magnetic latitude, an accuracy of a few hundred nanoteslas is obtained, which could explain, at least partially, the discrepancies reflected in the high-latitude disturbed conditions of Figure 4. Another possible cause could be related to the simplified treatment of induced currents below the Earth's surface (see section 4.1).

Figure 5a shows a period of intense Birkeland currents. The associated Hall conductance distribution consistently calculated by the TIE-GCM using the present approach (Figure 5c) shows enhancements in the dawn and dusk sectors matching the highest upward current densities in Figure 5a. Such conductances show a good qualitative and quantitative agreement with those obtained by use of the expressions of *Marklund et al*. [1988] (Figure 5d), with relative differences in the peak conductances around 9% in the predawn sector. Differences among the two methods possibly arise from their different nature. Note, for example, that the TIE-GCM conductivities depend on the geomagnetic field strength [e.g., *Richmond*, 1995b], which varies around the auroral zone, whereas the *Marklund et al*. [1988] formulas do not take this effect into account. The standard model (Figure 5b), on the contrary, shows a more uniform auroral enhancement that is insensitive to the AMPERE field-aligned current input by reason of the fact that it reflects average conditions for a given Kp.

Figure 6 again shows a satisfactory agreement between the present approach (6c and 6d) and that of *Marklund et al*. [1988] (6e and 6f), though in general the latter gives the highest values (15% to 30% higher) of the peak conductances. Such enhancements coincide with prominent upward field-aligned currents (Figures 6a and 6b) in the nightside auroral oval. Note in this context that the highest differences between the two models are generally observed in the Pedersen (rather than Hall) conductance.

Figures 6c–6f show conductivity enhancements in the premidnight sector, which is the zone where the discrete aurora dominates, as reported by *Newell et al*. [1996].

As stated above, the introduction of conductivities consistent with field-aligned currents has represented a modest improvement in terms of the ground magnetic perturbations with respect to the basic AMPERE-driven TIE-GCM [*Marsal et al*., 2012]. A possible reason for this could be connected with the fact that the conductance enhancements introduced by the present approach, though they are in reasonable agreement with the model of *Marklund et al*. [1988], are relatively local in nature (see Figures 5 and 6) and are usually limited in time to a few tens of minutes. Such localized conductance modifications must produce a correspondingly small improvement to the model agreement with ground magnetic data with respect to the basic AMPERE-driven TIE-GCM.

The second possibility for the abovementioned modest improvement could be related to the neglect of protons in the present approach. *Galand and Richmond* [2001] analyzed the contribution of this component and showed that it can be significant at particular times and locations. Its mean energy is considerably larger than its electron counterpart, though the associated energy flux is much weaker in general. This leads to some modification of the auroral conductance and, in consequence, of the electric potential; however, because the relative change is quite small on average, the effect on magnetic perturbations is not expected to be important.

The third possibility could be related to the fact that the present formulation for the energy flux, based on *Zhang and Paxton* [2008], depends on the Kp index solely, whereas *Korth et al*. [2014] show a dependence of that quantity on the IMF orientation. On the other hand, this latter paper points out that *Knight's* [1973] formulation

is more suitable at the afternoon upward R1 sector, meaning that the relation of Birkeland currents to mean energy and energy flux in that zone would apply even below the Zhang-Paxton threshold.

As stated above, the effect of dispersive Alfvén waves [e.g., *Chaston et al.*, 2003] in electron acceleration and precipitation has also been disregarded in the present formulation of the discrete aurora.

The last possibility could again be connected with the limited resolution of both AMPERE data and the TIE-GCM itself: unlike the diffuse aurora, discrete auroral events are features with typical latitudinal thicknesses ranging from hundreds of meters to tens of kilometers (e.g., *Gurnett* [1972], based on satellite data, *Hargreaves* [1992], or *Prölss* [2004]), associated with characteristic energies up to several tens of keV. Furthermore, they undergo rapid temporal variations and appear to move at velocities up to a few tens km/s. Such small scales are far below the resolution not only of AMPERE satellites but also of the TIE-GCM grid and are thus likely to be smoothed out by the background surrounding conditions. It is suggested here that bombardment of the auroral upper atmosphere by highly accelerated particles would eventually produce localized ionization enhancements and conducting filament structures invisible to AMPERE but enabling Hall currents to flow, thus producing noticeable magnetic effects on the ground. This, along with the localized nature of the conductivity enhancements, could be a candidate responsible for the small sensitivity of the TIE-GCM in response to making ionospheric conductivities consistent with the AMPERE field-aligned current input.

5. Summary and Conclusions

Marsal et al. [2012] and *Blanch et al.* [2013] used for the first time real field-aligned current data to drive the high-latitude electrodynamics in an upper atmosphere general circulation model. The approach used in these papers has been extended here to include a feedback between the Birkeland currents and the ionospheric conductivity. Theory has been developed to yield expressions relating the Birkeland currents with the characteristics of the precipitating electron population, which is then introduced in the standard energy deposition code to calculate the conductivities. The idea behind this approach lies on the assumption that intense field-aligned currents flowing upward above the auroral zone ionosphere, corresponding to energetic electrons precipitating from the magnetosphere, are linked to known electric potential drops between these two regions [*Knight*, 1973]. Such accelerated electrons produce ionization when they hit the upper atmosphere, thus increasing the local conductivity. The resulting conductance distributions are shown to be in reasonable agreement with an existing model accounting for particle precipitation. Field-aligned current data provided by the AMPERE satellite mission prove suitable for this purpose when used as an input to the TIE-GCM model.

As in the model of *Marklund et al.* [1988], the conductivities are enhanced in regions of significant upward field-aligned currents. The agreement with that model is significant for both the Hall and Pedersen conductances, though the model presented here typically gives somewhat lower values.

Results have been presented concerning the ground magnetic perturbations for different scenarios comprising a variety of latitudes and levels of magnetic disturbance. The modeled ground magnetic variations show a substantial improvement of the present method with respect to the standard TIE-GCM in relative terms. However, the model is still far from complete in absolute terms. Recall in this context that the TIE-GCM is not intended for modeling magnetospheric current systems, and that currents induced in the ground are greatly simplified. The AMPERE spatial resolution is comparable to the size of the large-scale field-aligned structures; the overall configuration of these currents could also vary substantially during the time resolution of this data set as well. As a result, the Birkeland currents available from the AMPERE database could be missing some valuable information, especially during disturbed conditions. Other intrinsic limitations of the standard TIE-GCM are cited here: No account is made for the two-way coupling with the lower atmosphere in the lower boundary; use of arbitrary ionization rates and neglect of ion transport and metallic ions to calculate the nighttime E region; arbitrary eddy diffusion rates at low altitudes; neglect of the two-way coupling with the magnetosphere; and limited spatial resolution, especially at auroral latitudes.

The use of AMPERE data, fed into the model every 10 min, improves the temporal resolution of the TIE-GCM output. This results in a better representation of magnetic perturbations at increasingly high latitudes and disturbance levels, which is connected with the fact that the field-aligned currents introduced by the AMPERE driving are more relevant in these situations. For quiet conditions, the AMPERE-driven model introduces a significant level of noise.

Most of the improvement attained in reproducing the ground magnetic perturbations has its origin in the application of the AMPERE data in the TIE-GCM, rather than making the auroral conductivities consistent with field-aligned currents. Some reasons are summarized here:

1. The modeled conductance enhancements appear as spatially localized and temporally limited patches in the perturbed auroral zone. This restricts the area of ground magnetic influence of the altered currents consistent with such enhancements.
2. The real discrete aurora is often below the space and time resolution of the Iridium satellites. The associated conductivity enhancements could give rise to relatively narrow but considerably intense currents which would eventually produce a nonnegligible magnetic effect on the ground.
3. Assumption of the Zhang-Paxton averages as representative of the diffuse auroral threshold, neglect of the role of dispersive Alfvén waves in electron precipitation; assumption of accelerated Maxwellian distribution functions for the incoming electrons; neglect of protons in terms of auroral conductivity; or the use of the IGRF to trace the geomagnetic field lines between conjugate points in the ionosphere are further assumptions approximating the complex reality.

Future efforts will be focused on improving the intrinsic Earth conductivity model in the TIE-GCM and on simulating the main magnetospheric contribution. Also, the present study needs to be extended to include more observatories at high latitudes so as to make conclusions more robust. Comparison of ionospheric conductance distributions with observations deduced from ISR measurements will also be considered.

Appendix A

A1. Number Flux, Energy Flux, and Mean Energy of an Accelerated Maxwellian Distribution

The flux of electrons in the ionosphere precipitating from the magnetosphere base is expressed in terms of the number flux density f_s as

$$F_S = \int_{E_k=0}^{\infty} f_s(E_k) dE_k. \tag{A1}$$

Likewise, the energy flux and mean energy are, respectively,

$$Q = \int_{E_k=0}^{\infty} E_k f_s(E_k) dE_k, \tag{A2}$$

$$\overline{E} = \frac{Q}{F_S},$$

where the different terms are properly defined in section 3, and the integrals are evaluated in the ionosphere base.

Unlike a pure Maxwellian, however, the form of the flux density function f_s of a Maxwellian accelerated by a potential drop V ($= \Phi_I - \Phi_S \geq 0$) and submitted to a varying magnetic field is not straightforward. Energies below eV, for example, are forbidden, so that $f_s(E_k < eV) = 0$. Let $v_\parallel$ be the component of the electron velocity along the ambient magnetic field, taken positive downward, and $v_\perp$ the magnitude of its perpendicular component. It is convenient to write the number flux density in the velocity space as the product of the parallel velocity and the Maxwellian distribution function, $d_s(\vec{v})$ [*Knight*, 1973]:

$$f_s(\vec{v}) = v_\parallel d_s(\vec{v}) = v_\parallel N_S \left(\frac{m_e}{2\pi k T_S} \right)^{3/2} e^{\frac{eV}{kT_S} - \frac{m_e \left(v_\parallel^2 + v_\perp^2 \right)}{2kT_S}}, \tag{A3}$$

and restrict the domain of integration of (A1) and (A2) to S_v (Figure A1), so that the electron flux, for example, is

$$F_S = \iiint_{S_v} f_s(\vec{v}) d^3 v,$$

where $d^3 v$ is the 3-D elementary volume in velocity space, and S_v accounts for only those ionospheric electrons originating in the magnetosphere base. This excludes the mentioned forbidden velocities, which can be deduced from the principle of conservation of energy and the first adiabatic invariant as follows:

The total energy of an electron in the magnetosphere base must be conserved in its way to the ionosphere base. Expressing the total energy, E_T, as the sum of its kinetic and potential components, E_k and E_p, one gets

$$E_T^S = E_k^S + E_p^S = E_k^S - e\Phi_S = E_k^I - e\Phi_I = E_k^I + E_p^I = E_T^I, \tag{A4}$$
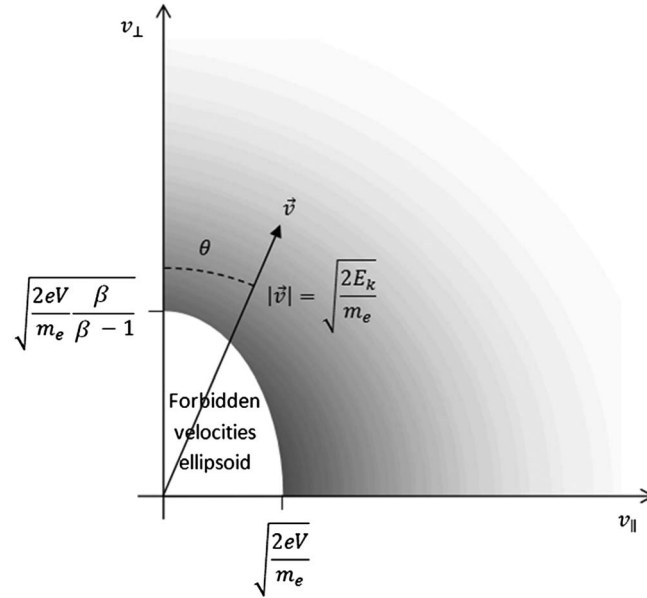
Figure A1. Representation of the distribution function $d_s(\vec{v})$ corresponding to an accelerated Maxwellian in the velocity space. Strictly speaking, a 3-D space should be considered with rotational symmetry around the $v_\parallel$ axis. Dark grey corresponds to higher electron densities. Note the semiellipsoid of forbidden velocities centered on the origin, where $d_s(\vec{v}) = 0$. The domain S_v corresponds to the semivolume outside the ellipsoid.

where S and I refer to the magnetosphere and ionosphere bases, respectively. On the other hand, from the first adiabatic invariant it is known that

$$\frac{\left(v_\perp^S\right)^2}{B_S} = \frac{\left(v_\perp^I\right)^2}{B_I}.\qquad(A5)$$

Let us now express the electron velocity components in terms of its energy and direction, $(1/2)m_e v_\perp^2 = (1/2)m_e(v\cos\theta)^2 = E_k\cos^2\theta$; $(1/2)m_e v_\parallel^2 = (1/2)m_e(v\sin\theta)^2 = E_k\sin^2\theta$, where θ [$-\pi/2, \pi/2$] is the complementary of the pitch angle, or angle that forms the electron velocity with the magnetic field line at each base, so that $\theta = 0$ in the direction perpendicular to the magnetic field, and $\theta = \pi/2$ for a field-aligned velocity facing the ionosphere. Thus, (A5) yields

$$\frac{E_k^S\cos^2\theta_S}{B_S} = \frac{E_k^I\cos^2\theta_I}{B_I}.\qquad(A6)$$

Making use of (A6), (A4) can be written as

$$-eV + E_k^I = E_k^S\left(\sin^2\theta_S + \cos^2\theta_S\right) = E_k^S\sin^2\theta_S + \frac{E_k^I\cos^2\theta_I}{\beta},$$

or equivalently,

$$-eV + E_k^I\left(1 - \frac{\cos^2\theta_I}{\beta}\right) = E_k^S\sin^2\theta_S.\qquad(A7)$$

The right-hand side of (A7) is a positively defined quantity, so a given value of E_k^I will be possible in the ionosphere if, and only if, it satisfies

$$E_k^I \geq eV\frac{\beta}{\beta - \cos^2\theta_I}.\qquad(A8)$$

Likewise, for an electron to plunge from the magnetosphere base, its velocity must necessarily face the ionosphere, which implies $\theta_I \geq 0$, thus defining the domain S_v. Hereafter, the subscript (and superscript) I is dropped, though it is implicit in the following instances of v, E_k, and θ, since these quantities are evaluated in the ionosphere base.

From (A3), the number of electrons in a volume d^3v of the velocity space is

$$d_s\left(\vec{v}\right)d^3v = N_S\left(\frac{m_e}{2\pi kT_S}\right)^{3/2}e^{\frac{eV}{kT_S} - \frac{m_e v^2}{2kT_S}}d^3v,$$

which, expressed in cylindrical coordinates, yields

$$d_s\left(\vec{v}\right)d^3v = N_S\left(\frac{m_e}{2\pi kT_S}\right)^{3/2}e^{\frac{eV}{kT_S} - \frac{m_e v^2}{2kT_S}}v^2\cos\theta\,dvd\theta d\phi$$

$$= \frac{N_S}{2}\left(\frac{1}{\pi kT_S}\right)^{3/2}e^{\frac{eV-E_k}{kT_S}}E_k^{1/2}\cos\theta\,dE_kd\theta d\phi.$$

The differential flux of electrons from the source region is thus

$$f_s\left(\vec{v}\right)d^3v = \frac{N_S}{\sqrt{2m_e}}\left(\frac{1}{\pi kT_S}\right)^{3/2}e^{\frac{eV-E_k}{kT_S}}E_k\sin\theta\cos\theta\,dE_kd\theta d\phi,$$

which yields a total number flux

$$F_S = \iiint_{S_v} f_s(\vec{v})\, d^3v = \frac{N_S}{\sqrt{2m_e}}\left(\frac{1}{\pi kT_S}\right)^{3/2} e^{\frac{eV}{kT_S}} \iiint_{S_{E\theta}} e^{-\frac{E_k}{kT_S}} E_k \sin\theta \cos\theta \, dE_k d\theta d\phi$$
$$= -N_S \sqrt{\frac{kT_S}{2\pi m_e}}\, e^{\frac{eV}{kT_S}} \iint_{S_{xy}} x e^{-x} dx dy,$$

(A9)

where the definitions $x = E_k/kT_S$, $y = \cos^2\theta$ have been used in the last step, and $S_{E\theta}$ and S_{xy} are the respective domains expressed in terms of the pairs of variables E_k, θ and x, y.

From (A8) it can be seen that kinetic energies above $eV\beta/(\beta - 1)$ are possible for any incidence angle θ. Between eV and $eV\beta/(\beta - 1)$, however, valid energies depend on the angle θ. In the latter interval, for a given E_k, the lower limit of the incidence angle, θ_L, fulfills

$$\cos^2\theta_L = \beta\left(1 - \frac{eV}{E_k}\right),$$

(A10)

which defines an ellipsoid in the velocity space, with semimajor axes $\sqrt{(2eV/m_e)\beta/(\beta - 1)}$ in the directions perpendicular to the magnetic field, and semiminor axis $\sqrt{2eV/m_e}$ along the magnetic field (Figure A1). This and the fact that $\theta \geq 0$ define the limits of integration in the last term of (A9):

$$\iint_{S_{xy}} x e^{-x} dx dy = \int_{x=\frac{eV}{kT_S}}^{\frac{eV}{kT_S}\frac{\beta}{\beta-1}} x e^{-x} dx \int_{y=\beta\left(1-\frac{eV}{xkT_S}\right)}^{0} dy + \int_{x=\frac{eV}{kT_S}\frac{\beta}{\beta-1}}^{\infty} x e^{-x} dx \int_{y=1}^{0} dy$$
$$= -\beta \int_{x=\frac{eV}{kT_S}}^{\frac{eV}{kT_S}\frac{\beta}{\beta-1}} x e^{-x}\left(1 - \frac{eV}{xkT_S}\right) dx - \int_{x=\frac{eV}{kT_S}\frac{\beta}{\beta-1}}^{\infty} x e^{-x} dx =$$

(A11)

$$= -\beta \int_{x=\frac{eV}{kT_S}}^{\frac{eV}{kT_S}\frac{\beta}{\beta-1}} x e^{-x} dx + \beta \frac{eV}{kT_S} \int_{x=\frac{eV}{kT_S}}^{\frac{eV}{kT_S}\frac{\beta}{\beta-1}} e^{-x} dx - \int_{x=\frac{eV}{kT_S}\frac{\beta}{\beta-1}}^{\infty} x e^{-x} dx$$

$$= \beta \frac{eV}{kT_S}\left(e^{-\frac{eV}{kT_S}} - e^{-\frac{eV}{kT_S}\frac{\beta}{\beta-1}}\right)$$

$$-\beta\left[\left(1 + \frac{eV}{kT_S}\right)e^{-\frac{eV}{kT_S}} - \left(1 + \frac{eV}{kT_S}\frac{\beta}{\beta-1}\right)e^{-\frac{eV}{kT_S}\frac{\beta}{\beta-1}}\right]$$

$$-\left(1 + \frac{eV}{kT_S}\frac{\beta}{\beta-1}\right)e^{-\frac{eV}{kT_S}\frac{\beta}{\beta-1}},$$

where the integrals in the last step have been evaluated by use of (A12) and (A13):

$$\int_{x=a}^{b} e^{-x} dx = e^{-a} - e^{-b},$$

(A12)

$$\int_{x=a}^{b} x e^{-x} dx = (1+a)e^{-a} - (1+b)e^{-b},$$

(A13)

$$\int_{x=a}^{b} x^2 e^{-x} dx = (2 + 2a + a^2)e^{-a} - (2 + 2b + b^2)e^{-b}.$$

(A14)

Simplifying (A11), one gets

$$F_S = -N_S \sqrt{\frac{kT_S}{2\pi m_e}}\, e^{\frac{eV}{kT_S}} \iint_{S_{xy}} x e^{-x} dx dy$$
$$= N_S \sqrt{\frac{kT_S}{2\pi m_e}}\left[\beta - (\beta - 1)e^{-\frac{eV}{kT_S}\frac{1}{\beta-1}}\right],$$

(A15)

which corresponds to the Maxwellian isotropic version of equations (5) of *Fridman and Lemaire* [1980] and (8) of *Janhunen and Olsson* [1998]. The energy flux is evaluated in a similar manner:

$$
Q = \iiint_{S_v} E_k f_s(\vec{v})\, d^3v = \frac{N_S E_k^2}{\sqrt{2m_e}}\left(\frac{1}{\pi k T_S}\right)^{3/2} e^{\frac{eV}{kT_S}} \iiint_{S_{E\theta}} e^{-\frac{E_k}{kT_S}} E_k^2 \sin\theta\cos\theta\, dE_k d\theta d\phi
$$

$$
= -N_S k T_S \sqrt{\frac{kT_S}{2\pi m_e}}\, e^{\frac{eV}{kT_S}} \iint_{S_{xy}} x^2 e^{-x}\, dx dy.
$$
(A16)

The integral in the last term of (A16) is

$$
\iint_{S_{xy}} x^2 e^{-x}\, dx dy =
$$

$$
= \int_{x=\frac{eV}{kT_S}}^{\frac{eV}{kT_S}\frac{\beta}{\beta-1}} x^2 e^{-x}\, dx \int_{y=\beta\left(1-\frac{eV}{xkT_S}\right)}^{0} dy + \int_{x=\frac{eV}{kT_S}\frac{\beta}{\beta-1}}^{\infty} x^2 e^{-x}\, dx \int_{y=1}^{0} dy
$$

$$
= -\beta\int_{x=\frac{eV}{kT_S}}^{\frac{eV}{kT_S}\frac{\beta}{\beta-1}} x^2 e^{-x}\, dx + \frac{\beta eV}{kT_S}\int_{x=\frac{eV}{kT_S}}^{\frac{eV}{kT_S}\frac{\beta}{\beta-1}} x e^{-x}\, dx - \int_{x=\frac{eV}{kT_S}\frac{\beta}{\beta-1}}^{\infty} x^2 e^{-x}\, dx
$$

$$
= -\beta\frac{eV}{kT_S}\left[\left(1+\frac{eV}{kT_S}\frac{\beta}{\beta-1}\right)e^{-\frac{eV}{kT_S}\frac{\beta}{\beta-1}} - \left(1+\frac{eV}{kT_S}\right)e^{-\frac{eV}{kT_S}}\right]
$$

$$
-\beta\left\{\left[2+\frac{2eV}{kT_S}+\left(\frac{eV}{kT_S}\right)^2\right]e^{-\frac{eV}{kT_S}} - \left[2+2\frac{eV}{kT_S}\frac{\beta}{\beta-1}+\left(\frac{eV}{kT_S}\frac{\beta}{\beta-1}\right)^2\right]e^{-\frac{eV}{kT_S}\frac{\beta}{\beta-1}}\right\}
$$

$$
-\left[2+2\frac{eV}{kT_S}\frac{\beta}{\beta-1}+\left(\frac{eV}{kT_S}\frac{\beta}{\beta-1}\right)^2\right]e^{-\frac{eV}{kT_S}\frac{\beta}{\beta-1}}
$$

$$
= -e^{-\frac{eV}{kT_S}}\left\{\beta\left(2+\frac{eV}{kT_S}\right) + \left[2-\beta\left(2+\frac{eV}{kT_S}\right)\right]e^{-\frac{eV}{kT_S}\frac{1}{\beta-1}}\right\},
$$

where use has been made of (A13) and (A14). The energy flux is thus

$$
Q = -kT_S N_S \sqrt{\frac{kT_S}{2\pi m_e}}\, e^{\frac{eV}{kT_S}} \iint_{S_{xy}} x^2 e^{-x}\, dx dy
$$

$$
= kT_S N_S \sqrt{\frac{kT_S}{2\pi m_e}}\left\{\beta\left(2+\frac{eV}{kT_S}\right) + \left[2-\beta\left(2+\frac{eV}{kT_S}\right)\right]e^{-\frac{eV}{kT_S}\frac{1}{\beta-1}}\right\},
$$
(A17)

which is the isotropic version of equations (6) of *Fridman and Lemaire* [1980] and (9) of *Janhunen and Olsson* [1998]. Finally, the mean energy is

$$
\bar{E} = \frac{Q}{F_S} = kT_S \frac{\beta\left(2+\frac{eV}{kT_S}\right) + \left[2-\beta\left(2+\frac{eV}{kT_S}\right)\right]e^{-\frac{eV}{kT_S}\frac{1}{\beta-1}}}{\beta-(\beta-1)e^{-\frac{eV}{kT_S}\frac{1}{\beta-1}}}
$$

$$
= kT_S \frac{2\left[\beta-(\beta-1)e^{-\frac{eV}{kT_S}\frac{1}{\beta-1}}\right]+\beta\frac{eV}{kT_S}\left(1-e^{-\frac{eV}{kT_S}\frac{1}{\beta-1}}\right)}{\beta-(\beta-1)e^{-\frac{eV}{kT_S}\frac{1}{\beta-1}}}
$$
(A18)

$$
= 2kT_S + \frac{eV}{1+\frac{1}{\beta}\left(e^{\frac{eV}{kT_S}\frac{1}{\beta-1}}-1\right)^{-1}},
$$

which corresponds to equation (5) in the main text and reduces to $2kT_S$ when $V=0$.

References

Anderson, B. J., H. Korth, C. L. Waters, D. L. Green, V. G. Merkin, R. J. Barnes, and L. P. Dyrud (2014), Development of large-scale Birkeland currents determined from the Active Magnetosphere and Planetary Electrodynamics Response Experiment, *Geophys. Res. Lett.*, *41*, 3017–3025, doi:10.1002/2014GL059941.

Blanch, E., S. Marsal, A. Segarra, J. M. Torta, D. Altadill, and J. J. Curto (2013), Space weather effects on Earth's environment associated to the 24–25 October 2011 geomagnetic storm, *Space Weather*, *11*, 153–168, doi:10.1002/swe.20035.

Blomberg, L. G., and G. T. Marklund (1988), The influence of conductivities consistent with field-aligned currents on high-latitude convection patterns, *J. Geophys. Res.*, *93*, 14,493–14,499, doi:10.1029/JA093iA12p14493.

Blomberg, L. G., and G. T. Marklund (1991), A numerical model of ionospheric convection derived from field-aligned currents and the corresponding conductivity, Rep. TRITA-EPP-91-03, Royal Inst. of Technol., Sweden.

Cattell, C., R. Lysak, R. B. Torbert, and F. S. Mozer (1979), Observations of differences between regions of current flowing into and out of the ionosphere, *Geophys. Res. Lett.*, *6*, 621–624, doi:10.1029/GL006i007p00621.

Cattell, C., J. Dombeck, W. Yusof, C. Carlson, and J. McFadden (2004), FAST observations of the solar illumination dependence of upflowing electron beams in the auroral zone, *J. Geophys. Res.*, *109*, A02209, doi:10.1029/2003JA010075.

Chaston, C. C., J. W. Bonnell, C. W. Carlson, J. P. McFadden, R. E. Ergun, and R. J. Strangeway (2003), Properties of small-scale Alfvén waves and accelerated electrons from FAST, *J. Geophys. Res.*, *108*(A4), 8003, doi:10.1029/2002JA009420.

Emery, B. A., R. G. Roble, E. C. Ridley, A. D. Richmond, D. J. Knipp, G. Crowley, D. S. Evans, F. J. Rich, and S. Maeda (2012), Parameterization of the ion convection and the auroral oval in the NCAR thermospheric general circulation models, *NCAR Tech*. *Note NCAR/TN-491 + STR*, ISSN Electronic Edition 2153–2400. [Available at http://nldr.library.ucar.edu/repository/collections/TECH-NOTE-000-000-000-856.]

Evans, D. S. (1974), Precipitating electron fluxes formed by a magnetic field aligned potential difference, *J. Geophys. Res.*, *79*, 2853–2858, doi:10.1029/JA079i019p02853.

Finlay, C. C., N. Olsen, and L. Tøffner-Clausen (2015), DTU candidate field models for IGRF-12 and the CHAOS-5 geomagnetic field model, *Earth Planets Space*, *67*, 114, doi:10.1186/s40623-015-0274-3.

Fridman, M., and J. Lemaire (1980), Relationship between auroral electrons fluxes and field aligned electric potential difference, *J. Geophys. Res.*, *85*(A2), 664–670, doi:10.1029/JA085iA02p00664.

Galand, M., and A. D. Richmond (2001), Ionospheric electrical conductances produced by auroral proton precipitation, *J. Geophys. Res.*, *106*(A1), 117–125, doi:10.1029/1999JA002001.

Germany, G. A., G. K. Parks, M. Brittnacher, J. Cumnock, D. Lummerzheim, J. F. Spann, L. Chen, P. G. Richards, and F. J. Rich (1997), Remote determination of auroral energy characteristics during substorm activity, *Geophys. Res. Lett.*, *24*, 995–998, doi:10.1029/97GL00864.

Gurnett, D. A. (1972), in *Critical Problems of Magnetospheric Physics*, edited by E. R. Dyer, p. 123, Nat. Acad. Sci., Washington, D. C.

Hagan, M. E., and J. M. Forbes (2002), Migrating and nonmigrating diurnal tides in the middle and upper atmosphere excited by tropospheric latent heat release, *J. Geophys. Res.*, *107*(D24), 4754, doi:10.1029/2001JD001236.

Hagan, M. E., and J. M. Forbes (2003), Migrating and nonmigrating semidiurnal tides in the upper atmosphere excited by tropospheric latent heat release, *J. Geophys. Res.*, *108*(A2), 1062, doi:10.1029/2002JA009466.

Hardy, D. A., M. S. Gussenhoven, R. Raistrick, and W. J. McNeil (1987), Statistical and functional representations of the pattern of auroral energy flux, number flux, and conductivity, *J. Geophys. Res.*, *92*(A11), 12,275–12,294, doi:10.1029/JA092iA11p12275.

Hargreaves, J. K. (1992), *The Solar-Terrestrial Environment: an Introduction to Geospace - the Science of the Terrestrial Upper Atmosphere, Ionosphere and Magnetosphere, Cambridge Atmospheric and Space Science Series*, vol. 7, Cambridge Univ. Press, U. K.

Heelis, R. A., J. K. Lowell, and R. W. Spiro (1982), A model of the high-latitude ionospheric convection pattern, *J. Geophys. Res.*, *87*(A8), 6339–6345, doi:10.1029/JA087iA08p06339.

Janhunen, P., and A. Olsson (1998), The current-voltage relationship revisited: Exact and approximate formulas with almost general validity for hot magnetospheric electrons for bi-Maxwellian and kappa distributions, *Ann. Geophys.*, *16*, 292–297, doi:10.1007/s00585-998-0292-6.

Knight, S. (1973), Parallel electric fields, *Planet. Space Sci.*, *21*(5), 741–750, doi:10.1016/0032-0633(73)90093-7.

Korth, H., L. Dyrud, B. J. Anderson, C. L. Waters, and R. J. Barnes (2010), AMPERE science data reduction and processing, Abstract SM11A-1692 presented at 2010 Fall Meeting, AGU.

Korth, H., Y. Zhang, B. J. Anderson, T. Sotirelis, and C. L. Waters (2014), Statistical relationship between large-scale upward field-aligned currents and electron precipitation, *J. Geophys. Res. Space Physics*, *119*, 6715–6731, doi:10.1002/2014JA019961.

Marklund, G. T., L. G. Blomberg, K. Stasiewicz, J. S. Murphree, R. Pottelette, L. J. Zanetti, T. A. Potemra, D. A. Hardy, and F. J. Rich (1988), Snapshots of high-latitude electrodynamics using Viking and DMSP F7 observations, *J. Geophys. Res.*, *93*(A12), 14,479–14,492, doi:10.1029/JA093iA12p14479.

Marsal, S., A. D. Richmond, A. Maute, and B. J. Anderson (2012), Forcing the TIEGCM model with Birkeland currents from the active magnetosphere and planetary electrodynamics response experiment, *J. Geophys. Res.*, *117*, A06308, doi:10.1029/2011JA017416.

Maus, S., C. Manoj, J. Rauberg, I. Michaelis, and H. Lühr (2010), NOAA/NGDC candidate models for the 11th generation International Geomagnetic Reference Field and the concurrent release of the 6th generation Pomme magnetic model, *Earth Planets Space*, *62*(10), 729–735, doi:10.5047/eps.2010.07.006.

McDiarmid, I. B., J. R. Burrows, and E. E. Budzinski (1975), Average characteristics of magnetospheric electrons (150 eV to 200 keV) at 1400 km, *J. Geophys. Res.*, *80*(1), 73–79, doi:10.1029/JA080i001p00073.

Mishin, V. M., S. B. Lunyushkin, D. S. Shirapov, and W. Baumjohann (1986), A new method for generating instantaneous ionospheric conductivity models using ground-based magnetic data, *Planet. Space Sci.*, *34*, 713, doi:10.1016/0032-0633(86)90125-X.

Newell, P. T., C. I. Meng, and K. M. Lyons (1996), Suppression of discrete aurora by sunlight, *Nature*, *381*, 766–767, doi:10.1038/381766a0.

Newell, P. T., T. Sotirelis, and S. Wing (2009), Diffuse, monoenergetic, and broadband aurora: The global precipitation budget, *J. Geophys. Res.*, *114*, A09207, doi:10.1029/2009JA014326.

Ni, B., R. M. Thorne, R. B. Horne, N. P. Meredith, Y. Y. Shprits, L. J. Chen, and W. Li (2011a), Resonant scattering of plasma sheet electrons leading to diffuse auroral precipitation: 1. Evaluation for electrostatic electron cyclotron harmonic waves, *J. Geophys. Res.*, *116*, A04218, doi:10.1029/2010JA016232.

Ni, B., R. M. Thorne, N. P. Meredith, R. B. Horne, and Y. Y. Shprits (2011b), Resonant scattering of plasma sheet electrons leading to diffuse auroral precipitation: 2. Evaluation for whistler mode chorus waves, *J. Geophys. Res.*, *116*, A04219, doi:10.1029/2010JA016233.

Olsen, N. (1996), Magnetospheric contributions to geomagnetic daily variations, *Ann. Geophys.*, *14*, 538–544, doi:10.1007/s00585-996-0538-0.

Paxton, L. J., D. Morrison, D. J. Strickland, M. G. McHarg, Y. Zhang, B. Wolven, H. Kil, G. Crowley, A. B. Christensen, and C.-I. Meng (2000), The use of far ultraviolet remote sensing to monitor space weather, COSPAR, *Adv. Space Res.*, *31*(4), 813–818, doi:10.1016/S0273-1177(02)00886-4.

Prölss, G. W. (2004), *Physics of the Earth's Space Environment. An Introduction*, Springer, Berlin.

Rees, M. H. (1963), Auroral ionization and excitation by incident energetic electrons, *Planet. Space Sci.*, *11*(10), 1209–1218, doi:10.1016/0032-0633(63)90252-6.

Richmond, A. D. (1974), The computation of magnetic effects of field-aligned magnetospheric currents, *J. Atmos. Terr. Phys.*, *36*, 245–252, doi:10.1016/0021-9169(74)90044-0.

Richmond, A. D. (1995a), Ionospheric electrodynamics using magnetic apex coordinates, *J. Geomagn. Geoelectr.*, *47*, 191–212.

Richmond, A. D. (1995b), Ionospheric electrodynamics, in *Handbook of Atmospheric Electrodynamics*, vol. II, edited by H. Volland, pp. 249–290, CRC Press, Boca Raton, Fla.

Richmond, A. D., and A. Maute (2013), Ionospheric electrodynamics modeling, in *Modeling the Ionosphere-Thermosphere System*, *Geophys. Monogr. Ser.*, vol. 201, edited by J. Huba, R. Schunk, and G. Khazanov, pp. 57–71, AGU, Washington, D. C., doi:10.1002/9781118704417.ch6.

Richmond, A. D., E. C. Ridley, and R. G. Roble (1992), A thermosphere/ionosphere general circulation model with coupled electrodynamics, *Geophys. Res. Lett.*, *19*(6), 601–604, doi:10.1029/92GL00401.

Robinson, R. M., R. R. Vondrak, K. Miller, T. Dabbs, and D. Hardy (1987), On calculating ionospheric conductances from the flux and energy of precipitating electrons, *J. Geophys. Res.*, *92*(A3), 2565–2569, doi:10.1029/JA092iA03p02565.

Roble, R. G., and M. H. Rees (1977), Time-dependent studies of the aurora: Effects of particle precipitation on the dynamic morphology of ionospheric and atmospheric properties, *Planet. Space Sci.*, *25*, 991–1010, doi:10.1016/0032-0633(77)90146-5.

Roble, R. G., and E. C. Ridley (1987), An auroral model for the NCAR thermospheric general circulation model (TGCM), *Ann. Geophys.*, *5A*(6), 369–382.

Roble, R. G., E. C. Ridley, A. D. Richmond, and R. E. Dickinson (1988), A coupled thermosphere/ionosphere general circulation model, *Geophys. Res. Lett.*, *15*(12), 1325–1328, doi:10.1029/GL015i012p01325.

Sabaka, T. J., N. Olsen, R. H. Tyler, and A. Kuvshinov (2015), CM5, a pre-Swarm comprehensive geomagnetic field model derived from over 12 yr of CHAMP, Ørsted, SAC-C and observatory data (2015), *Geophys. J. Int.*, *200*(3), 1596–1626, doi:10.1093/gji/ggu493.

Solomon, S. C., and L. Qian (2005), Solar extreme-ultraviolet irradiance for general circulation models, *J. Geophys. Res.*, *110*, A10306, doi:10.1029/2005JA011160.

Spiro, R. W., P. H. Reiff, and L. J. Maher Jr. (1982), Precipitating electron energy flux and auroral zone conductances—An empirical model, *J. Geophys. Res.*, *87*(A10), 8215–8227, doi:10.1029/JA087iA10p08215.

Torta, J. M., S. Marsal, and M. Quintana (2014), Assessing the hazard from geomagnetically induced currents to the entire high-voltage power network in Spain, *Earth Planets Space*, *66*, 87, doi:10.1186/1880-5981-66-87.

Vickrey, J. F., R. R. Vondrak, and S. J. Matthews (1981), The diurnal and latitudinal variations of auroral zone ionospheric conductivity, *J. Geophys. Res.*, *86*(A1), 65–75, doi:10.1029/JA086iA01p00065.

Wallis, D. D., and E. E. Budzinski (1981), Empirical models of height integrated conductivities, *J. Geophys. Res.*, *86*(A1), 125–137, doi:10.1029/JA086iA01p00125.

Wiltberger, M., R. S. Weigel, W. Lotko, and J. A. Fedder (2009), Modeling seasonal variations of auroral particle precipitation in a global-scale magnetosphere-ionosphere simulation, *J. Geophys. Res.*, *114*, A01204, doi:10.1029/2008JA013108.

Zhang, Y., and L. J. Paxton (2008), An empirical *Kp*-dependent global auroral model based on TIMED/GUVI FUV data, *J. Atmos. Sol. Terr. Phys.*, *70*(8), 1231–1242, doi:10.1016/j.jastp.2008.03.008.